

## Maximizing thermoelectric performance in SnTe through strategic co-doping, nanostructuring, and topological insights

Peramaiyan Ganesan<sup>\*1</sup>, Chandra Shekar Gentapogu<sup>1</sup>, Sidharth Duraisamy<sup>1</sup>, Phillip Wu<sup>1</sup>, Gwo-Tzong Huang<sup>1</sup>, Muhammad Yusuf Fakhri<sup>1</sup>, Kuei-Hsien Chen<sup>2</sup>, Yang-Yuan Chen<sup>1</sup>, Maw-Kuen Wu<sup>\*1</sup>

<sup>1</sup>Institute of Physics, Academia Sinica

<sup>2</sup>Institute of Atomic and Molecular Sciences, Academia Sinica

### Methods:

High-purity Sn shots (99.999%), Te chunks (99.999%), Mg chunks (99.99%), Bi chunks (99.999%), and Ag shots (99.999%) were meticulously weighed to achieve the stoichiometric ratio of SnTe and SnTe doped with Ag, Mg, and Bi. These materials were handled in an argon-filled glove box, maintaining oxygen and water levels below 0.20 ppm. Approximately 10 g of raw materials were loaded into a glassy-carbon crucible and placed into a quartz tube. This assembly was evacuated and flame-sealed under a pressure of  $\sim 2.75 \times 10^{-6}$  torr. The samples were gradually heated to 1223 K over 12 hours and maintained at this temperature for an additional 10 hours before allowing the furnace to cool naturally. The resultant ingot was hand-ground and placed into a stainless steel ball milling jar, undergoing milling at 600 rpm for 3 hours. The resulting powders were then loaded into a graphite die with a diameter of about 12.7 mm and sintered using Spark Plasma Sintering (SPS) at 823 K under 40 MPa pressure for 10 minutes. The final pellet exhibited a density of approximately 99% compared to the theoretical density. Single crystals were grown by Bridgman technique. These pellets were subsequently cut into suitable sizes for thermoelectric transport measurements.

### Powder and synchrotron X-ray diffraction

SPS-sintered samples of SnTe, doped with Ag, Mg, and Bi, were finely ground and loaded onto a silicon holder. The X-ray wavelength used was 1.5406 Å. The FullProf suite software was employed to refine the obtained PXRD patterns through Rietveld analysis. Synchrotron X-ray diffraction was carried out on Ag, Bi-doped SnTe and Ag, Mg, and Bi-doped SnTe at different temperatures to gain deeper insights into the impurity phases and temperature dependency. Crystal planes were identified by Laue X-ray diffraction measurement.

## **Scanning transmission electron microscopy (STEM)**

Polycrystalline specimens were prepared using a focused ion beam (FIB) technique via the FEI Nova-200. Subsequent microscopic investigations were conducted with the JEM-2100F microscope, operating at 300 kV, from Japan JEOL Co. The morphology of the bulk samples was observed through a scanning electron microscope (SEM, JEOL, Japan).

## **Electrical and thermal transport measurements**

We employed the ULVAC ZEM-3 (M10) for resistivity and Seebeck coefficient measurements, maintaining an uncertainty within 5 to 10%. Thermal diffusivity was assessed using the laser flash diffusivity method. Polycrystalline samples, cut into square-like slabs with dimensions of 12.7 mm × 12.7 mm × (1.7-2.2) mm, were carbon-coated and measured with the Netzsch LFA 457 instrument. The total thermal conductivity was calculated using the formula  $\kappa_{\text{tot}} = D \cdot C_p \cdot d$ , where  $D$  represents thermal diffusivity,  $C_p$  is the heat capacity derived from the Dulong-Petit law, and ' $d$ ' is the sample density determined by the Archimedes method. The uncertainty for thermal conductivity was estimated at approximately 5-6%. The overall uncertainty for the final ZT, derived from both the power factor and thermal conductivity, was about 10-15%. For low-temperature thermoelectric transport measurements (10-300 K), including thermal conductivity, Seebeck coefficient, resistivity, and specific heat capacity, we used a Quantum Design Physical Property Measurement System (PPMS). Hall transport measurements were also conducted using PPMS to estimate carrier concentration and mobility. The carrier concentration ( $n_h$ ) was calculated using the formula:  $n_h = 1/eR_H$ , where  $e$  is the elementary charge and  $R_H$  is the Hall coefficient. The carrier mobility ( $\mu_h$ ) was determined using the formula:  $\mu_h = \sigma/n_h e$ , where  $\sigma$  is the electrical conductivity,  $n_h$  is the carrier concentration of holes, and  $e$  is the elementary charge.

## **Thermogravimetric analysis**

Thermogravimetric analysis was performed under argon atmosphere for 30 °C to 900 °C under 5 C per minute .

## **Estimation of weighted mobility**

To estimate the weighted mobility, we used the experimentally obtained Seebeck coefficient and electrical resistivity as proposed by Snyder et al<sup>1</sup>.

$$\mu_W = 331 \frac{cm^2}{Vs} \left( \frac{m\Omega cm}{\rho} \right) \left( \frac{T}{300K} \right)^{3/2} \left[ \frac{\exp \left[ \frac{|S|}{k_B/e} - 2 \right]}{1 + \exp \left[ -5 \frac{|S|}{k_B/e} - 1 \right]} + \frac{\frac{3 |S|}{\pi^2 k_B/e}}{1 + \exp \left[ 5 \frac{|S|}{k_B/e} - 1 \right]} \right] \dots (1)$$

In equation (1),  $\mu_W$  is the weighted mobility,  $\rho$  is the electrical resistivity (m $\Omega$ -cm), T is the absolute temperature (Kelvin), S is the Seebeck coefficient ( $\mu$ V/K), and  $k_B/e = 86.3 \mu$ V/K.

### Low-temperature heat capacity fitting analysis

To accurately fit the  $C_p/T$  versus  $T^2$  data for  $Sn_{0.86}Bi_{0.06}Ag_{0.03}Mg_{0.08}Te$ , we employed a combined Debye-Einstein model<sup>2</sup>. This model effectively accounts for the phonon contributions to the heat capacity across both low and high-temperature regimes, providing a more comprehensive understanding of the thermodynamic properties of the material.

$$\frac{C_p}{T} = \gamma + \beta T^2 + \sum_n \left( A_n (\Theta_{En})^2 \cdot (T^2)^{-\frac{3}{2}} \cdot \frac{e^{-\frac{\Theta_{En}}{T}}}{\left( e^{-\frac{\Theta_{En}}{T}} - 1 \right)^2} \right) \dots (2)$$

$$\beta = C(12\pi^4 N_A k_B/5)(\Theta_D)^{-3} \dots (3)$$

$$C = 1 - \sum_n A_n / (3NR) \dots (4)$$

In the above equation,  $\gamma$  denotes the electronic contribution, and  $\beta T^2$  corresponds to the Debye mode. In equation (3),  $N_A$ ,  $k_B$  and  $\Theta_D$  are Avogadro number, Boltzmann constant and Debye temperature, respectively. N is the number of atoms, and R is the gas constant in equation (4). In the third term of equation 2,  $A_n$  is the prefactor, and  $\Theta_{En}$  is the Einstein temperature for the  $n^{\text{th}}$  mode. The fitted parameters are given in Table S2.

### Magnetization measurements

Magnetization measurements were performed on pristine SnTe single crystals along the (010) and (111) directions with a magnetic field strength of up to 7 T using a vibrating sample magnetometer (VSM). The resulting magnetization curves exhibited clear de Haas-an Alphen (dHvA) oscillations. The linear background of the M-H data was subtracted to isolate the oscillatory magnetization. The  $\Delta M$  vs  $1/H$  plot displayed periodic oscillations. The MH measurements were performed at various temperatures: 3, 4, 5, 6, and 7 K. Based on the

Onsager relation,  $F = (\phi_0/2\pi^2)A_F$ , the Fermi surface cross-sectional ( $A_F$ ) is calculated. Lifshitz-Kosevich (LK)<sup>3</sup> formula describes the pure oscillatory magnetization ( $\Delta M$ ).

$$\Delta M \propto B^{1/2} R_T R_D R_S \cos [2\pi(\frac{F}{B} + \gamma - \delta)] \dots(5)$$

where,  $R_T = \alpha T m^*/B \sinh(\alpha T m^*/B)$ ,  $R_D = \exp(-\alpha T_D m^*/B)$ , and  $R_S = \cos(\pi g m^*/m_0)$ . Here,  $m_0$  and  $m^*$  are free electron mass and effective cyclotron mass, respectively.  $T_D$  is Dingle temperature, and  $\alpha = (2\pi^2 k_B m_0)/(\hbar e)$ . From the  $\ln\{\Delta M[1-\exp(-2\alpha m^* T/B)]/T\}$  vs.  $T$  plot, the effective cyclotron mass is estimated. The plot of  $\ln(\Delta M B^{1/2} / \sinh(\alpha m^* T/B))$  vs. inverse magnetic field yields the Dingle temperature ( $T_D$ ), and the corresponding electron scattering time is calculated by using the relation,  $\tau = \hbar / 2\pi k_B T_D$ . The Fermi wave vector ( $K_F$ ) is calculated

using the relation  $\sqrt{\left(\frac{A_F}{\pi}\right)}$  and the Fermi velocity is estimated using a  $\frac{\hbar K_F}{m^*}$  relation.

### Average ZT calculation

The average figure of merit is calculated using the following relation<sup>4</sup>

$$ZT_{avg} = \frac{1}{T_h - T_c} \int_{T_c}^{T_h} ZT dT \dots(6)$$

### Density of states (DOS) effective mass calculation

By utilizing the carrier concentrations derived from the Hall effect and the experimentally obtained Seebeck coefficient ( $S$ ), we can calculate the effective mass ( $m_d^*$ )<sup>5</sup>.

$$m_d^* = 0.857 \left(\frac{300K}{T}\right) m_e \left(\frac{n}{10^{20} cm^{-3}}\right)^{2/3} \frac{\left[3 \left(\exp\left[\frac{|S|}{k_B/e} - 2\right] - 0.17\right)\right]^{2/3}}{\left[1 + \exp\left[-5 \left(\frac{|S|}{k_B/e} - \frac{k_B/e}{|S|}\right)\right]\right]} + \frac{\frac{|S|}{k_B/e}}{\left[1 + \exp\left[5 \left(\frac{|S|}{k_B/e} - \frac{k_B/e}{|S|}\right)\right]\right]} \dots(6)$$

where  $m_d^*$  is the DOS effective mass. It is also referred to as the Seebeck effective mass ( $m_s^*$ ),  $m_e$  is the rest mass of an electron,  $n=n_H r_H$  is the carrier concentration ( $n_H$  is the Hall carrier concentration and  $r_H$  is the Hall factor),  $k_B$  is the Boltzmann constant,  $e$  is the charge of the electron, and  $S$  is the Seebeck coefficient.

### Debye- Callaway model- $\kappa_L$ fitting analysis

To understand the influence of different phonon scattering mechanisms on the ultralow  $\kappa_L$  of (Ag, Mg, and Bi) co-doped SnTe, we fitted the measured  $\kappa_L$  of  $\text{Sn}_{0.86}\text{Bi}_{0.06}\text{Ag}_{0.03}\text{Mg}_{0.08}\text{Te}$  below 300 K using the Debye–Callaway model<sup>6–8</sup>.

$$\kappa_L = \frac{k_B}{2\pi^2 v_s} \left( \frac{k_B T}{\hbar} \right)^3 \int_0^{\theta_D/T} \frac{x^4 e^x}{\tau^{-1} (e^x - 1)^2} dx \quad \dots(7)$$

where  $x = \hbar\omega/(k_B T)$  is the reduced phonon energy,  $\hbar$  is the reduced Plank constant,  $k_B$  is the Boltzmann constant,  $v_s$  is the average acoustic velocity,  $\theta_D$  is the Debye temperature.

This model provides valuable insights into how various phonon scattering mechanisms contribute to the significant reduction in thermal conductivity, enhancing our comprehension of the material's performance. The relaxation time for the  $\text{Sn}_{0.86}\text{Bi}_{0.06}\text{Ag}_{0.03}\text{Mg}_{0.08}\text{Te}$  encompasses the Umklapp process, grain boundary scattering, point defects, nanoprecipitates, stacking faults, and resonant scattering, as described by the following equation:

$$\tau^{-1} = \tau_U^{-1} + \tau_B^{-1} + \tau_{PD}^{-1} + \tau_{NP}^{-1} + \tau_{SF}^{-1} + \tau_{RES}^{-1} \quad (8)$$

The relaxation time for the Umklapp process can be expressed as:

$$\tau_U^{-1} \approx \frac{\hbar \gamma^2}{M v^2 \theta_D} \omega^2 T \exp\left(-\frac{\theta_D}{3T}\right) \quad (9)$$

In the above equation,  $\hbar$  is Plank's reduced constant,  $\gamma$  is the Gruneisen parameter,  $M$  is the average mass of an atom,  $v$  is the average sound velocity,  $\theta_D$  is the Debye temperature, and  $\omega$  is the Debye frequency.

The relaxation time influenced by grain boundary can be simplified as:

$$\tau_{GB}^{-1} = \frac{v}{L} \quad (10)$$

$L$  is the grain size.

The relaxation time for the point defects is described as

$$\tau_{PD}^{-1} = F\Gamma = \frac{\omega^4 V}{4\pi v^3} \Gamma \quad (8)$$

$$\Gamma = \Gamma_M + \Gamma_S \quad (9)$$

$V$  is the volume per atom,  $v$  the average sound velocity, and  $\Gamma$  the disorder scaling parameter, which depends on mass and strain field fluctuations. The mass fluctuations are quantified by  $\Gamma_M$  which takes into account the average mass of each of the sublattices and the strain field fluctuations by  $\Gamma_S$ . The explicit relations of  $\Gamma_M$  and  $\Gamma_S$  are given as:

$$\Gamma_M = \sqrt{\sum_i f_i \left(\frac{\Delta M}{M}\right)^2} \quad (10)$$

$$\Gamma_S = \sqrt{\sum_i f_i \left(\frac{\Delta R}{R}\right)^2} \quad (11)$$

where  $f_i$  is the atomic fraction of the  $i^{\text{th}}$  type of impurity,  $\Delta M$  is the difference in mass between the impurity and the host atom and  $M$  is the average mass of the host atom.

The relaxation time influenced by precipitates can be simplified as:

$$\tau_{NP}^{-1} = v \left[ (2\pi R^2)^{-1} + \left( \pi R^2 \frac{4}{9} \left(\frac{\Delta D}{D}\right)^2 \left(\frac{\omega R}{v}\right)^4 - 1 \right)^{-1} \right]^{-1} N_p \quad (12)$$

$R$  is the average diameter of the precipitates,  $D$  is the matrix density,  $\Delta D$  is the density difference between the matrix and precipitates,  $N_p$  is the density of precipitates.

Table S1 Fitted parameters to the specific heat capacity data ( $C_p/T$  versus  $T^2$  data) using the Debye-Einstein model for  $\text{Sn}_{0.86}\text{Bi}_{0.06}\text{Ag}_{0.03}\text{Mg}_{0.08}\text{Te}$

Parameters	Debye-Einstein Model
$\gamma$ ( $10^{-3} \text{ J mol}^{-1} \text{ K}^{-2}$ )	16.68±1.24
$\beta$ ( $10^{-5} \text{ J mol}^{-1} \text{ K}^{-2}$ )	1.58±0.450
A1 ( $\text{J mol}^{-1} \text{ K}^{-1}$ )	12.64±0.39

A2 (J mol <sup>-1</sup> K <sup>-1</sup> )	29.06±0.41
Θ <sub>E1</sub> (K)	53.00±0.48
Θ <sub>E2</sub> (K)	104.47±1.34
Θ <sub>D</sub> (K)	127.7 K
R <sup>2</sup>	0.99997
χ <sup>2</sup>	1.9244×10 <sup>-6</sup>

Table S2 Fitted parameters to the lattice thermal conductivity ( $\kappa_L$ ) using the Debye-Callaway model for Sn<sub>1.03</sub>Te and Sn<sub>0.86</sub>Bi<sub>0.06</sub>Ag<sub>0.03</sub>Mg<sub>0.08</sub>Te

Parameters	Debye-Callaway Model	
	Sn <sub>1.03</sub> Te	Sn <sub>0.86</sub> Bi <sub>0.06</sub> Ag <sub>0.03</sub> Mg <sub>0.08</sub> Te
Sound velocity(m/s)	1800	1610
Grain size (m)	4.81×10 <sup>-7</sup>	1.02×10 <sup>-6</sup>
Umklapp scattering (s/K)	8.52×10 <sup>-19</sup>	1.21×10 <sup>-20</sup>
Point defect scattering(s <sup>3</sup> )	-	5.33×10 <sup>-43</sup>
Stacking faults (s)	1.58×10 <sup>-17</sup>	9.99×10 <sup>-16</sup>
Resonance energy scattering(s <sup>-1</sup> )	-	1.131×10 <sup>36</sup>
Angular frequency (rad/s)	1.833×10 <sup>13</sup>	1.365×10 <sup>13</sup>
The number density of nanoprecipitates(m <sup>-3</sup> )	-	3.09×10 <sup>26</sup>
χ <sup>2</sup>	0.9822	0.9793

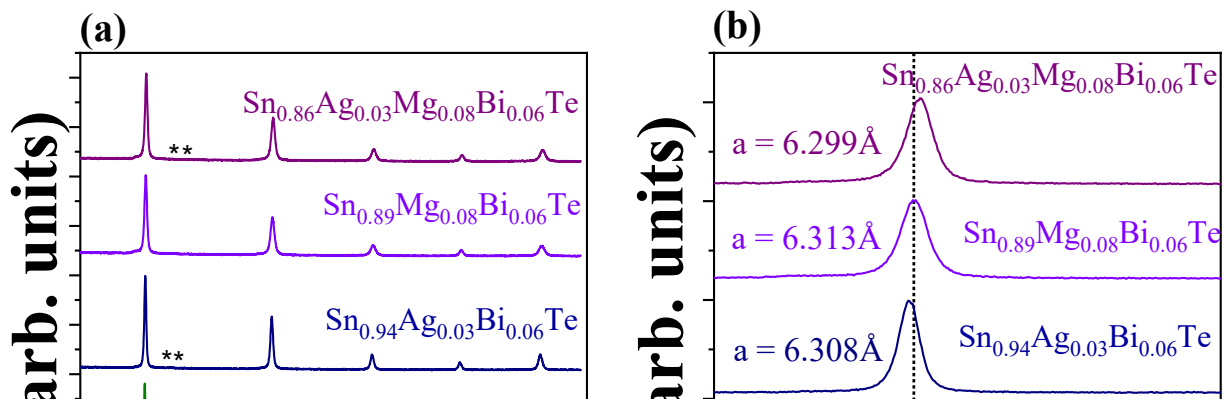


**Figure S1 (a) X-ray diffraction (XRD) patterns of various compositions of Sn, Ag, Mo, Bi, and Te. The diffraction patterns show how different compositions affect the crystal structure. The asterisk (\*\*) indicates the Sn impurities. (b) Detailed view of the XRD patterns focusing on the peak around 27-31 degrees  $2\theta$  for the same compositions. The lattice constants 'a' are provided next to each pattern, showing slight variations in lattice parameters with different compositions.**

Electron Image 3

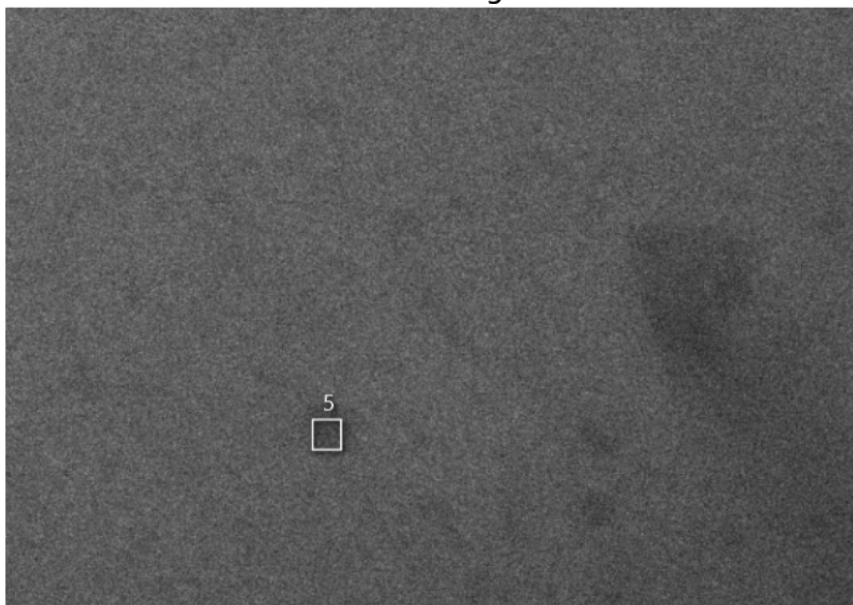


**Figure S2 a) STEM image of Ag, Mg, and Bi doped SnTe, highlighting the microstructural features of the material. b) EDS plot taken from the precipitate observed in the STEM image, confirming the presence of MgTe precipitate. The EDS analysis provides a detailed elemental composition, indicating significant peaks for Mg, Te, and other dopants, which corroborates the formation of MgTe within the SnTe matrix. The size of the MgTe precipitates varies from 1.3 nm to 10 nm.**

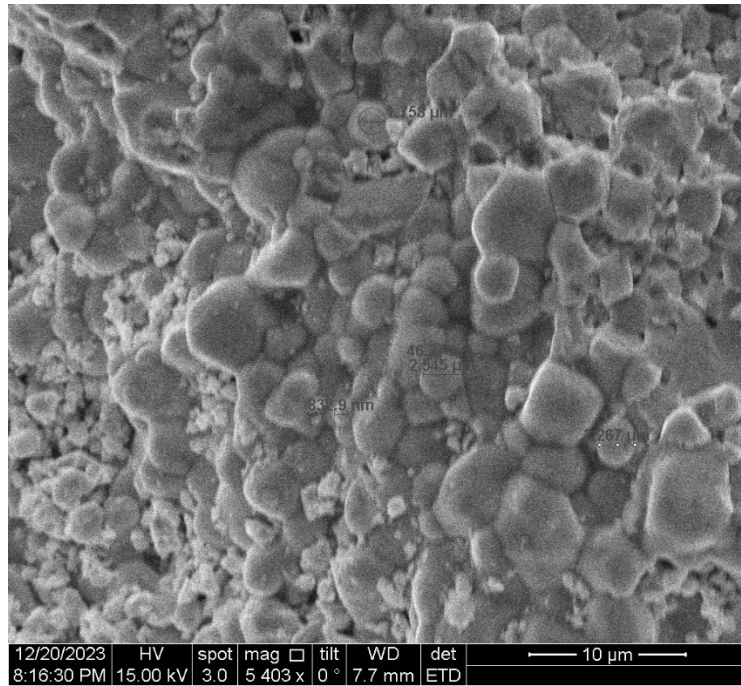
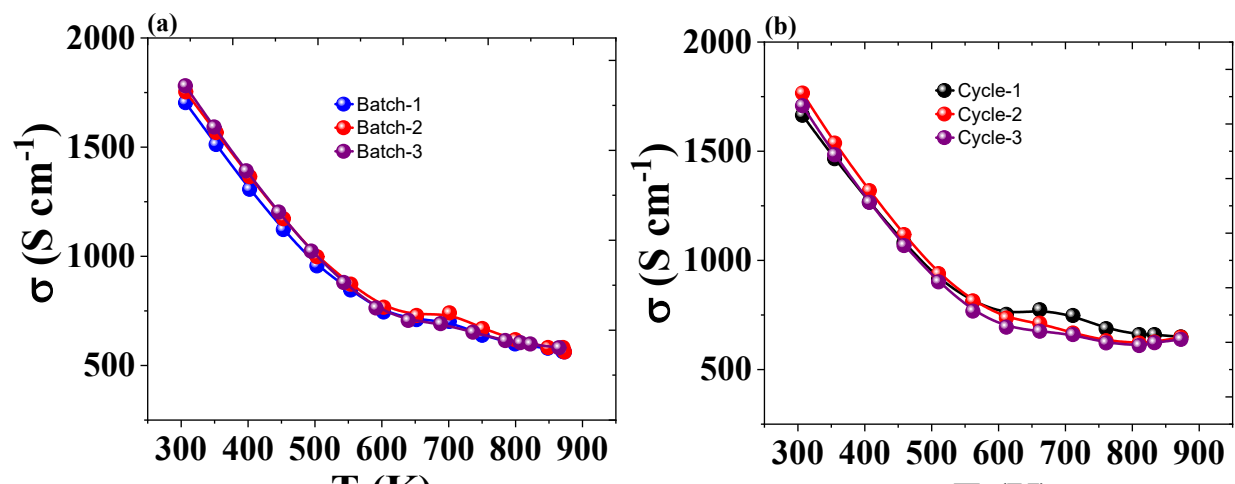


Figure S3 Scanning electron microscopic image of  $\text{Sn}_{0.86}\text{Ag}_{0.03}\text{Mg}_{0.08}\text{Bi}_{0.06}\text{Te}$  sample



**Figure S4 Repeatability and reproducibility of  $\text{Sn}_{0.86}\text{Bi}_{0.06}\text{Ag}_{0.03}\text{Mg}_{0.08}\text{Te}$  sample.**

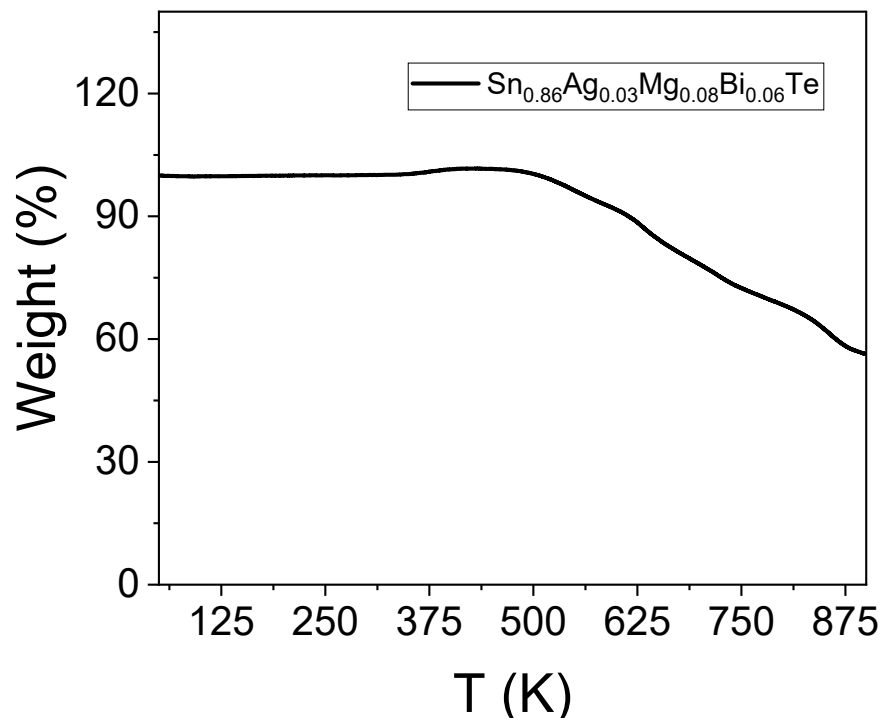
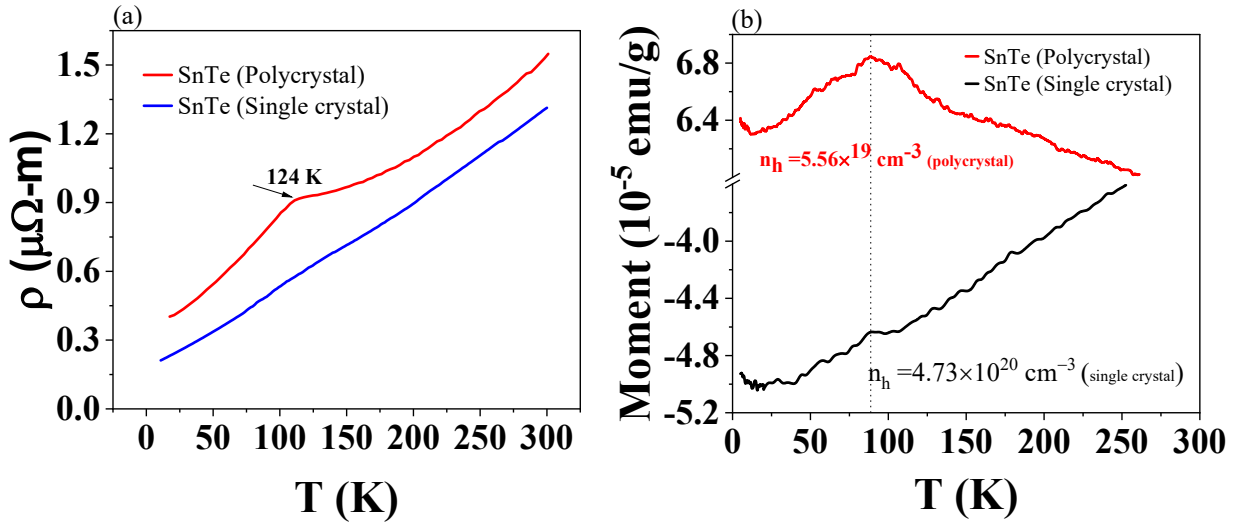
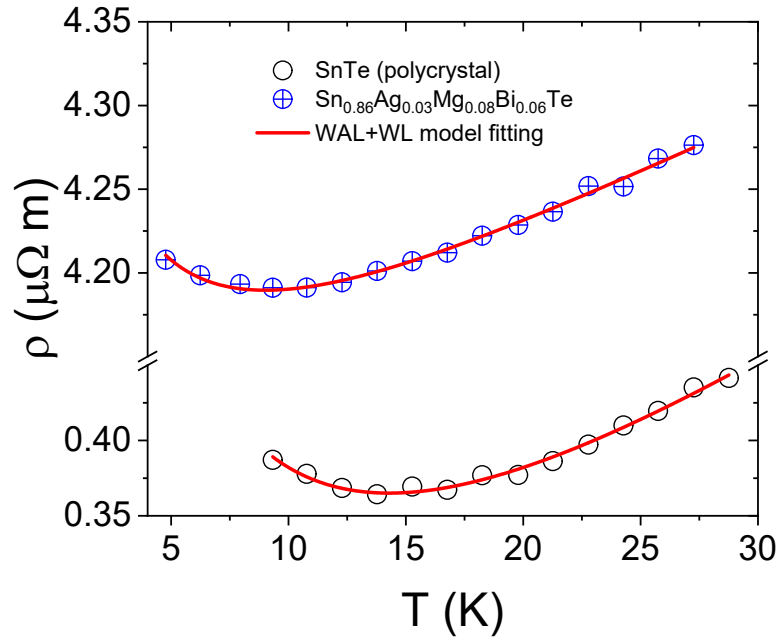


Figure S5 Thermogravimetric curve of of  $\text{Sn}_{0.86}\text{Bi}_{0.06}\text{Ag}_{0.03}\text{Mg}_{0.08}\text{Te}$  sample.



**Figure S6 Temperature-dependent resistivity curves of single and polycrystalline SnTe. The polycrystalline SnTe shows a clear phase transition at 114 K, marked by a distinct peak in the resistivity curve, whereas the single crystal sample does not exhibit a similar clear peak. This difference could be due to the increased phonon scattering and defect interactions in the polycrystalline sample, enhancing the visibility of the transition. This transition correlates with the cubic to rhombohedral phase shift, contributing to the complex behavior in resistivity and thermal properties. This transition at 112 K in the MT (magnetization vs. temperature) curve for the polycrystalline sample aligns well with our resistivity findings. It indicates that the cubic to rhombohedral phase transition is indeed affecting the magnetic properties. The fact that it's less pronounced in the single crystal but still visible suggests that the structural transition impacts both types but is more accentuated in polycrystalline due to increased scattering at grain boundaries and defects. The negative magnetization in single crystal SnTe within the measured temperature range is likely due to a combination of higher carrier concentration, fewer defects, and strong spin-orbit coupling. These factors collectively contribute to the observed magnetic behavior, distinguishing it from the polycrystalline sample.**



**Figure S7** The plot shows the resistivity ( $\rho$ ) as a function of temperature ( $T$ ) for pristine polycrystalline SnTe and  $\text{Sn}_{0.86}\text{Ag}_{0.03}\text{Mg}_{0.08}\text{Bi}_{0.06}\text{Te}$  samples. The resistivity data is fitted using the model,  $\rho(T) = \rho_0 + A\sqrt{T} - B \ln(T)$ , where  $\rho_0$  represents the residual resistivity,  $A$  corresponds to weak antilocalization (WAL) effects, and  $B$  corresponds to weak localization (WL) effects.

## References

- 1 G. J. Snyder, A. H. Snyder, M. Wood, R. Gurunathan, B. H. Snyder and C. Niu, *Advanced Materials*, 2020, **32**, 2001537.
- 2 S. Roychowdhury, T. Ghosh, R. Arora, M. Samanta, L. Xie, N. K. Singh, A. Soni, J. He, U. V Waghmare and K. Biswas, *Science (1979)*, 2021, **371**, 722–727.
- 3 D. Shoenberg, *Magnetic Oscillations in Metals*, Cambridge University Press, 1984.
- 4 H. S. Kim, W. Liu, G. Chen, C.-W. Chu and Z. Ren, *Proceedings of the National Academy of Sciences*, 2015, **112**, 8205–8210.
- 5 G. J. Snyder, A. Pereyra and R. Gurunathan, *Adv Funct Mater*, 2022, **32**, 2112772.
- 6 F. Li, X. Liu, S.-R. Li, X.-F. Zhang, N. Ma, X.-J. Li, X.-Y. Lin, L. Chen, H. Wu and L.-M. Wu, *Energy Environ Sci*, 2024, **17**, 158–172.
- 7 J. Callaway and H. C. von Baeyer, *Physical Review*, 1960, **120**, 1149–1154.
- 8 J. Callaway, *Physical Review*, 1959, **113**, 1046–1051.